PAPER

Check for updates

A novel COOH–GO–COOH–MWNT/pDA/AuNPs based electrochemical aptasensor for detection of AFB₁†

Pengfei Wang,‡[ab] Bin Luo,‡[a] Ke Liu,[a] Cheng Wang,[a] Hongtu Dong,[a] Xiaodong Wang,[a] Peichen Hou[a] and Aixue Li ⓘ *[ab]

Aflatoxin B₁ (AFB₁), one of the most common mycotoxins in food matrixes, has been identified as the most toxic contaminant with mutagenic, teratogenic, immunosuppressive, and carcinogenic effects. In this study, an electrochemical aptamer sensor was developed for the on-site detection of AFB₁. Carboxylated graphene oxide (COOH–GO) and carboxylated multi-walled carbon nanotubes (COOH–MWNT) nanocomposites, dopamine polymers (pDA) and gold nanoparticles (AuNPs) were used to enhance the electrochemical activity and the biocompatibility of the screen-printed electrodes (SPE). Once AFB₁ was captured by the aptamer immobilized on the electrode surface, the redox current of $[Fe(CN)_6]^{3-/4-}$ decreased. Therefore, the binding of aptamer (Apt) and AFB₁ can be reflected by the change of the peak current. The as-prepared sensor showed a wide detection range of 0.1 fg ml⁻¹–100 pg ml⁻¹ and a low detection limit of 15.16 ag ml⁻¹. It is also simple and low-cost, which shows great potential in practical application.

1 Introduction

Aflatoxin (AFT) is a secondary metabolite produced by *Aspergillus flavus*. It is also a class of destructive mycotoxins.[1] More than ten kinds of aflatoxins have been isolated and identified. Among the aflatoxin family, aflatoxin B₁ (AFB₁) has the most potent virulent, mutagenic and carcinogenic effects.[2] It can lead to the contamination of a large number of food and agricultural products, which has the most extensive impact on human life and causes the greatest loss.[3,4] The European Commission has set 2 ppb or 6.4 nM as the maximum allowable level of AFB₁ in various grains and agricultural by-products.[5,6] Therefore, the development of a rapid and sensitive AFB₁ detection method at various stages of food and agricultural production has become urgent.

To date, various analytical methods such as high-performance liquid chromatography,[7] tandem mass spectrometry,[8] and enzyme-linked immunosorbent assay (ELISA),[9] *etc.*, have been developed for the detection of AFB₁. However, these methods require expensive equipment and professional operators, and take a lot of time to process samples, which limit their application for rapid and on-site analysis. Immunosensors are

a very promising AFB₁ detection technology, but their cost is still high due to the application of antibodies.

Aptamers are short oligonucleotide sequences or short polypeptides screened *in vitro*. Compared with antibodies, aptamers have higher thermal, chemical stability and lower synthesis costs.[10–12] At present, many aptamer sensors capable of rapid detection in the field have been developed, showing great potential in the safe detection of AFB₁.[13–24] For example, Abnous *et al.* developed a π-shaped structure composed of an aptamer and its complementary strand as a physical barrier on the electrode surface.[25] When AFB₁ is detected, the π-shaped structure is broken down by exonuclease I, and a change in peak current can be observed. Wang *et al.* developed a short AFB₁ aptamer, which was modified with a blue (MB) tag at the 3′ end and then immobilized on the electrode surface to recognize the toxin. In the process of AFB₁ binding to aptamer, MB is close to the electrode surface, and the peak current increases.[26] However, for these reported aptamer sensors, complex manufacturing process, cumbersome reaction steps, and expensive enzyme are usually needed. Therefore, developing simple and effective aptamer sensors for AFB₁ is still required in practical applications.

In this study, in order to develop a sensor that can be widely used in practical production, screen-printed electrodes (SPEs) with low cost and mature manufacturing technology were selected. Because of the good catalytic activity and excellent electrical conductivity, carbon-based nanomaterials, such as graphene oxide (GO) and carbon nanotubes (MWNT), have attracted extensive attention. However, if applied alone, the

[a] Intelligent Equipment Research Center, Beijing Academy of Agriculture and Forestry Sciences, Beijing 100097, China. E-mail: aixueli_2021@163.com; liax@nercita.org.cn

[b] College of Agricultural Engineering, Jiangsu University, Jiangsu 212000, China

‡ This author contributed equally to this work.

aggregation or restacking of GO sheets that inevitably occurs due to the strong π–π interactions. And the high performance of the CNTs cannot be obtained if they could not uniformly disperse to form a network sufficient for electrical conductivity. Recent studies have reported that the above problems could be solved by introducing MWNTs between the GO nanosheets.[27–29] In the composite of GO–MWNT, the good dispersion of MWNTs can avoid the aggregation of GO sheets, and GO nanosheets also directly disperse MWNTs as "surfactant" to form a three-dimensional networks. Moreover, the carboxylated graphene oxide (COOH–GO) and carboxylated multi-walled carbon nanotubes (COOH–MWNT) have better hydrophilicity, biocompatibility, and carboxyl functional groups, which will further enhance the performance of sensor. Due to the good synergistic effect, the combination of COOH–GO and COOH–MWNT can often lead to better electrochemical performance, which has been confirmed in our previous work.[30,31] Therefore, in this work, the carboxylated GO (COOH–GO) and carboxylated MWNT (COOH–MWNT) were also used to improve the performance of the sensor. Polydopamine (pDA) has the advantages of abundant functional groups, excellent biocompatibility and easy preparation, and has been widely used in different fields including cell sensing, molecular imprinting, and creation of biocompatible layers., *etc.* It also has been reported to effectively amplify charge transfer of mediators.[32,33] Therefore, pDA was applied to enhance the electrochemical activity and the biocompatibility of the electrode in our work. Gold nanoparticles (AuNPs) were also used not only because they have excellent catalytic activity and electrochemical stability, but also because they can firmly bind to –SH contained aptamers. Finally, a short 28-mer DNA aptamer was immobilized on the electrodes, which was used to specifically recognize AFB$_1$. This aptamer has been reported to have high binding affinity to AFB$_1$, and it undergoes a conformational change to form a hairpin structure upon binding with AFB$_1$.[34,35] The as-prepared

electrochemical AFB$_1$ aptamer sensor not only has low limit of detection (LOD), wide linear detection range, specific recognition ability and stability, but also is simple and low cost, which has a wide range of practical application prospects.

2 Material and methods

2.1 Reagents

One short anti-AFB$_1$ aptamer (sequence 5′-SH-(CH$_2$)$_6$-GCACGTGTTGTCTCTCTGTGTCTCGTGC-3′), named as SH-Apt, were purified and synthesized by Sangon Biotech (Shanghai, China). Aflatoxin B$_1$ (AFB$_1$), Aflatoxin B$_2$ (AFB$_2$), ochratoxin B (OTB), Zearalenone (ZON), fumonisins B$_1$ (FB$_1$), fumonisins B$_2$ (FB$_2$), and Deoxynivalenol (DON) were purchased from Aladdin Chemistry Co., Ltd (Shanghai, China). Nafion solution (5 wt%), dopamine hydrochloride, gold (III) chloride trihydrate (HAuCl$_4$·H$_2$O), 6-Mercapto-1-hexanol (MCH/98 wt%), and Tris-(2-carboxyrthyl) phosphine hy-drochloride (TCEP/0.5 M) were purchased from Sigma-Aldrich Co., Ltd. (St. Louis, USA). Carboxylated graphene oxide (COOH–GO), and Carboxylated carbon nanotubes (COOH–MWNT) were purchased from XFNANO materials Tech Co, Ltd. The other reagents are of analytical grade, and solutions are prepared by dissolving these reagents in double-distilled water.

2.2 Apparatus

All measurements were carried out on a CHI760E workstation purchased from Shanghai Chenhua Instrument Co., Ltd., China. The different morphologies of the electrodes were characterized using an electron microscope (SEM) and an energy dispersive analysis (EDS) system (ZEISS, SEM 500, Germany) The SPE purchased from Ningbo Mxense Biotechnology Co., Ltd. consisted of a working electrode, a carbon-based counter electrode, and an Ag/AgCl reference electrode.
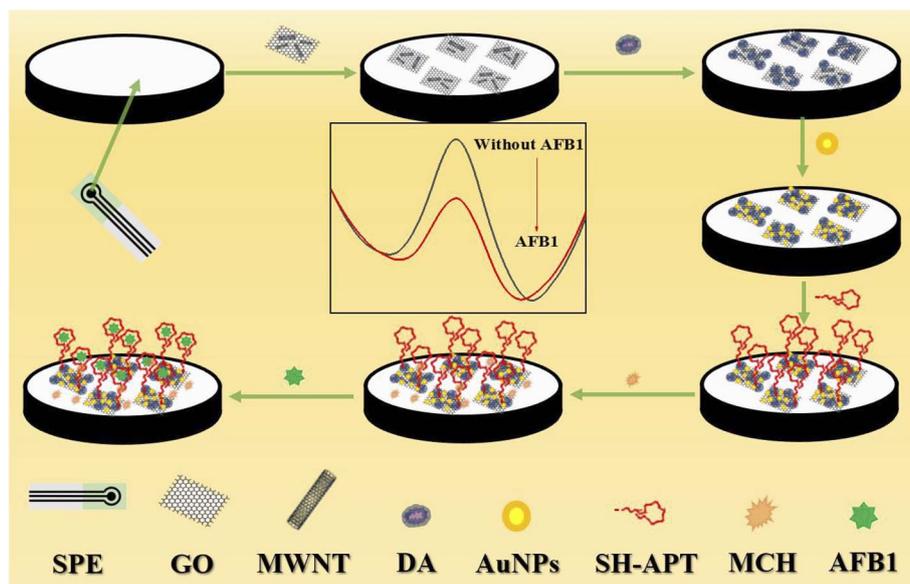
Scheme 1 Schematic representation of the sensor fabrication.

2.3 Preparation of COOH–GO–COOH–MWNT nanocomposite

The COOH–GO–COOH–MWNT nanocomposite is composed of COOH–GO (1 mg ml^{-1}) with COOH–MWNT (1 mg ml^{-1}). Nafion (0.5%) was added to the mixture. The mixed solution is ultra-sonicated for two hours and a homogeneous dispersion was obtained.

2.4 Construction of electrochemical aptamer sensor

The fabrication process of the aptamer sensor was shown in Scheme 1. Firstly, the cleaned bare electrode was scanned in PBS buffer (0.01 M, pH 7.5, containing 0.1 M KCl) at a constant potential of 1.7 V for 180 s. Secondly, 4 μl of COOH–GO–COOH–MWNT nanocomposites were evenly drop-coated on the working electrode, thirdly, after dried, 5 mM dopamine (DA) solution was polymerized on the electrode at 80 mV with a scan rate of $-0.6 \text{ v} \sim 0.6 \text{ v}$. Fourthly, the treated electrodes were immersed in a 0.1 mg ml^{-1} HAuCl$_4$ aqueous solution, and a constant potential of -1.3 v was maintained for 1000 s to deposit AuNPs on the working electrode. Fifthly, the aptamer was immobilized on the electrode by Au–S bond. The aptamers were mixed with the TCEP solution (0.01 mM) for 2 hours before use to reduce the oxidized aptamer, and the aptamer were incubated with the electrode for 1 hour at 25 °C. Finally, the electrodes were incubated with 2 mM MCH for two hours at 25 °C to prevent non-specific binding of AFB$_1$. PBS buffer was used to wash the electrode after each modified step.

2.5 Measurement procedure

The aptamer sensor was incubated with 3 μl of different concentrations of AFB$_1$ solutions (0.1 fg ml^{-1}–100 pg ml^{-1}) for 1 h at 25 °C. Then PBS buffer (0.01 M, pH 7.5, containing 0.1 M KCl) was used to remove unbound toxin. Measurements were performed using differential pulse voltammetry (DPV) in the presence of 5 mM K$_3$ [Fe(CN)$_6$]/K$_4$ [Fe(CN)$_6$] (1 : 1) mixture as a redox probe in 0.01 M PBS (pH 7.5, containing 0.1 M KCl). The pulse period, width and amplitude of the DPV method were 0.2 s, 50 ms and 50 mv, respectively.

3 Results and discussion

3.1 Characterizations of the fabrication of the aptamer sensor

In this study, the topographical features of the working electrode were observed by SEM. Fig. 1A shows the surface morphology of the bare electrode. The surface of the electrode is clean and presents uniform granular carbon material. After modifying by COOH–GO–COOH–MWNT nanocomposite (Fig. 1B), a three-dimensional network structure formed by tubular COOH–MWNT and lamellar COOH–GO can be observed, which can increase the active area and conductivity of the electrode greatly. After DA polymerization occurred on the electrode (Fig. 1C), obvious particles appeared on the three-dimensional network structure, which can further increase the active area and conductivity of the electrode. Fig. 1D shows the surface morphology of AuNPs/pDA/COOH–GO–COOH–
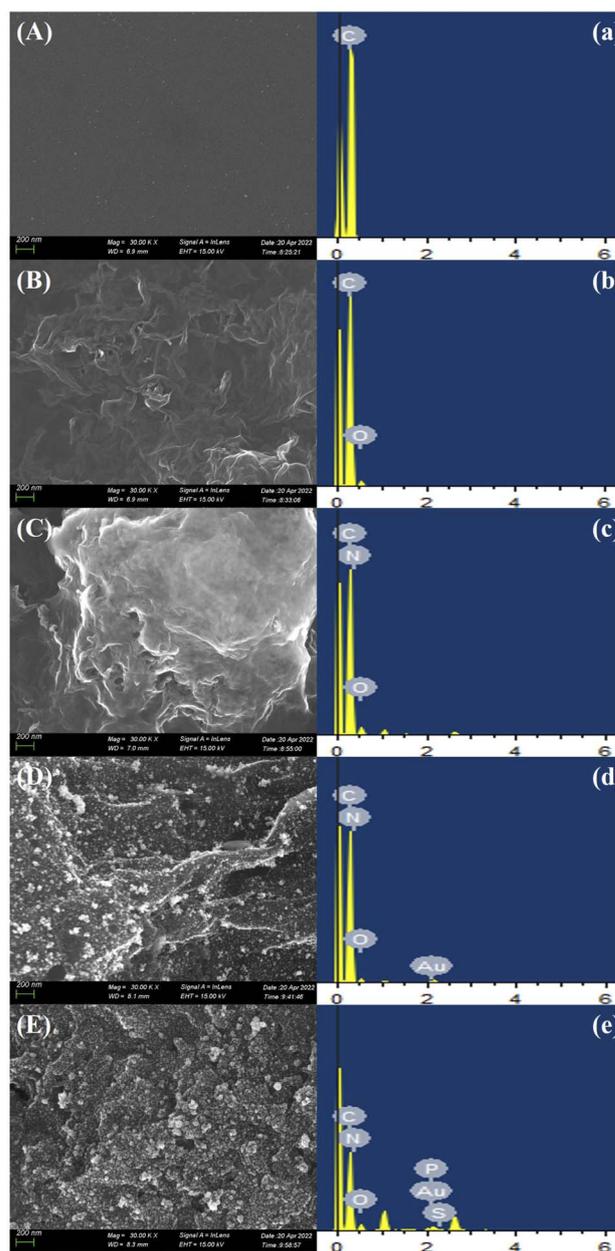

Fig. 1 SEM (A–E) and EDS (a–e) analysis of bare SPE, COOH–GO–COOH–MWNT/SPE, pDA/ COOH–GO–COOH–MWNT/SPE, Au/pDA/COOH–GO–COOH–MWNT/SPE, and MCH/SH-Apt/Au/pDA/COOH–GO–COOH–MWNT/SPE.

MWNT/SPE modified electrode, and the densely arranged gold nanoparticles (AuNPs) can be clearly observed, which can not only improve the catalytic activity of the electrode, but also provide binding sites for aptamers. After binding with the aptamers and MCH (Fig. 1E), the film on the surface of electrode becomes denser.

EDS was also used to verify the modification steps of the sensor. The EDS test results of the bare electrodes are shown in Fig. 1a. The main element in this step is C, which is due to the fact that the surface of the SPE electrode is composed of carbon material. After modification of COOH–GO–COOH–MWNT nanocomposite on the electrode (Fig. 1b), in addition to the
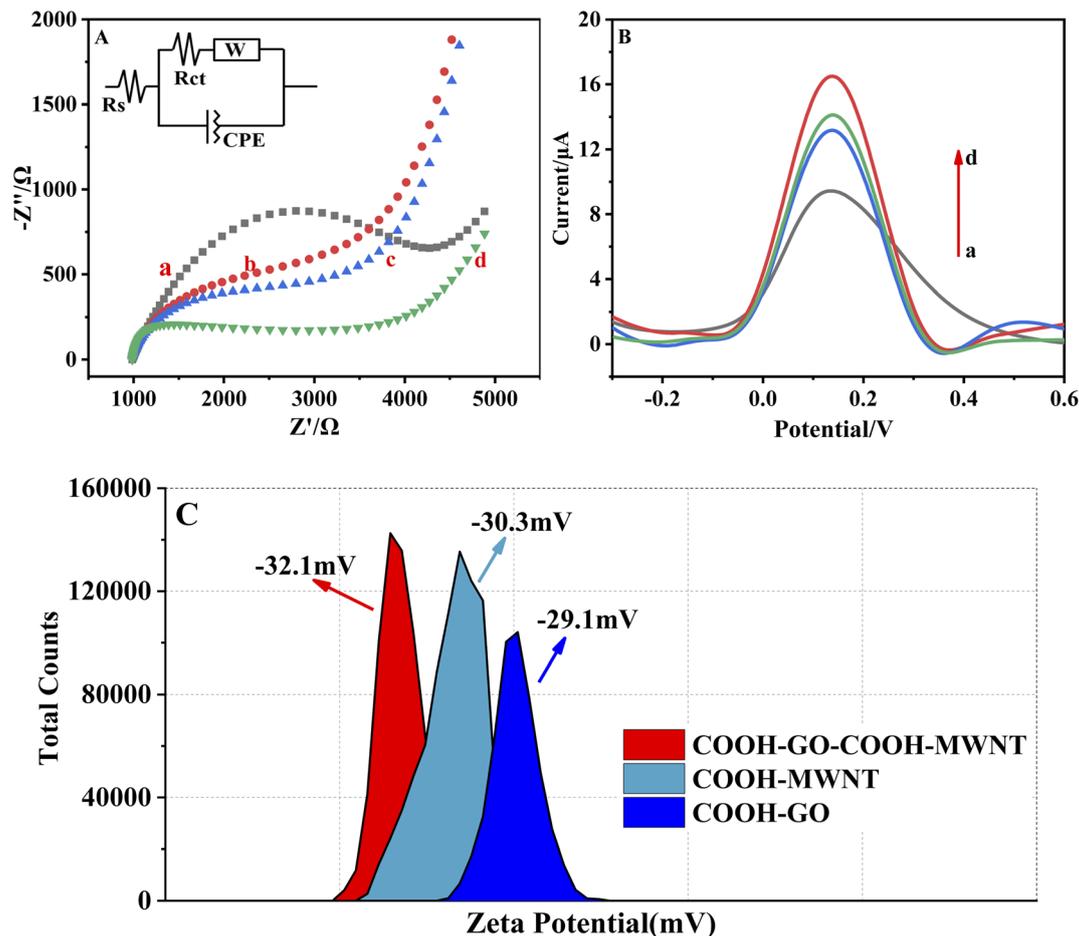
Fig. 2 EIS (A), DPV (B) and ZETA potential (C) characterization: (a), bare electrode, (b), COOH–GO/SPE, (c), COOH–MWNT/SPE, and (d), COOH–GO–COOH–MWNT/SPE. The EIS and DPV measurement were performed in the presence of 5 mM $[Fe(CN)_6]^{3-/4-}$ in 0.01 M PBS (pH 7.5, containing 0.1 M KCl).

original C element, O element was found, because COOH–GO contains a large number of oxygen-containing groups, and COOH–MWNT contains a large number of carboxyl groups. In Fig. 1c, in addition to C and O element, N element is found, which is attributed to the fact that the aggregated DA contains N element. After modification of AuNPs (Fig. 1d), Au element is added in the EDS result, which verifies the success of modification of AuNPs. After the aptamers and MCH were incubated with the electrode (Fig. 1e), P and S elements were added in the EDS spectrogram, because DNA aptamers contains P element and sulfhydryl, and MCH also contains sulfhydryl.

Electrochemical Impedance Spectroscopy (EIS), Differential Pulse Voltammetry (DPV) and ZETA potentials were all used to characterize COOH–GO/SPE, COOH–MWNT/SPE and COOH–GO–COOH–MWNT/SPE. As shown in Fig. 2A, the impedance arc of the three modified electrodes is smaller than that of the bare electrode, and the impedance arc of the COOH–GO–COOH–MWNT/SPE (d) is significantly smaller than that of COOH–GO/SPE (b) and COOH–MWNT/SPE (c). In Fig. 2B, the DPV response of COOH–GO–COOH–MWNT/SPE (d) is significantly higher than that of COOH–GO/SPE (b) and COOH–MWNT/SPE (c). These two results suggested that the conductivity of COOH–GO–

COOH–MWNT composite was superior than COOH–GO or COOH–MWNT alone. Meanwhile, ZETA potential was also used to characterize these three materials. The ZETA potential value of COOH–GO, COOH–MWNT, and COOH–GO–COOH–MWNT nanocomposites were −29.1, −30.3, and −32.1 respectively. ZETA potential value of −30 mV was regarded as the dividing point from incipient instability to moderate stability for carbon-based nanomaterials dispersion.[36] The COOH–GO–COOH–MWNT nanocomposites was more stable, which consistent with previous studies, that is, MWNTs can avoid the aggregation of GO sheets and GO nanosheets also help to disperse MWNTs. Therefore, in our work, we choose COOH–GO–COOH–MWNT to modify the electrode.

EIS was also used to characterize individual steps of sensor modification. As shown in Fig. 3A, a relatively large arc was obtained at the bare electrode, indicating that the resistance of the bare electrode was large. When adding COOH–GO–COOH–MWNT nanocomposites on the working electrode, the arc became smaller due to that the active area and conductivity of the electrode can be enhanced by the modification of the COOH–GO–COOH–MWNT nanocomposite. When pDA and AuNPs was modified on the electrode, the impedance value
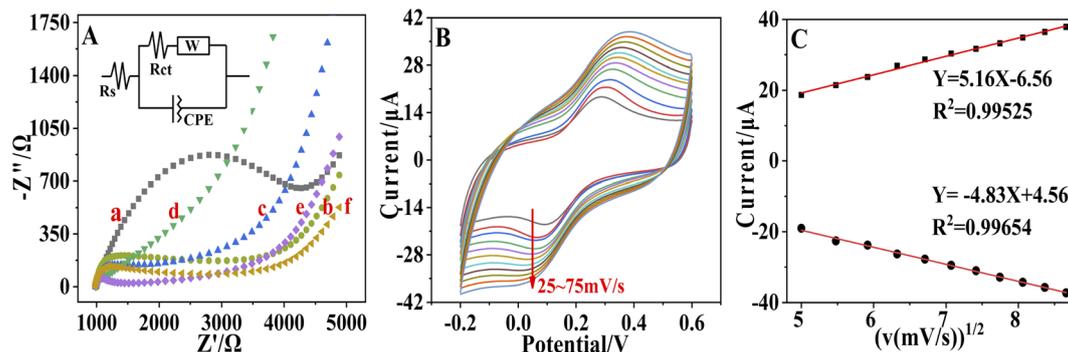
Fig. 3 (A) Nyquist plot of electrode modification, (a–f) are bare SPE, COOH−GO−COOH−MWNT/SPE, pDA/COOH−GO−COOH−MWNT/SPE, Au/pDA/COOH−GO−COOH−MWNT/SPE, SH-Apt/Au/pDA/COOH−GO−COOH−MWNT/SPE, and MCH/SH-Apt/Au/pDA/COOH−GO−COOH−MWNT/SPE. (B) CV of the sensor in the presence of 5 mM [Fe(CN)$_6$]$^{3−/4−}$ in 0.01 M PBS (pH 7.5, containing 0.1 M KCl) at scan rates ranging from 25 to 75 mV s^{-1}. (C) Linear fitting of the oxidized peak current (I_{pa}) and reduced peak current (I_{pc}) versus the square root of the scan rate ($v^{1/2}$).

decreased further as pDA and AuNPs can enhance the active area and conductivity of the electrode further. When the aptamer was incubated with the electrode, the arc became larger due to the non-conductive property of the aptamer. After incubating with the blocker MCH, the resistance further increased due to that MCH was also unconducive. Fitting by a simple circuit (the inset in Fig. 3A), the R_{ct} values for each modification steps were respectively 3.31 kΩ, 2.52 kΩ, 2.33 kΩ, 1.3 kΩ, 1.51 kΩ and 1.83 kΩ for the bare SPE, COOH−GO−COOH−MWNT/SPE, pDA/COOH−GO−COOH−MWNT/SPE, Au/pDA/COOH−GO−COOH−MWNT/SPE, SH-Apt/Au/pDA/COOH−GO−COOH−MWNT/SPE, and MCH/SH-Apt/Au/pDA/COOH−GO−COOH−MWNT/SPE modified electrode. The EIS result confirmed the successfully modification of the electrode.

This study also explored the effect of scan rate of cyclic voltammetry scan on electrode performance. The prepared MCH/SH-Apt/Au/pDA/GO−MWNT/SPE electrode was placed in the presence of 5 mM [Fe(CN)$_6$]$^{3−/4−}$ in 0.01 M PBS (pH 7.5, containing 0.1 M KCl) and the scan rate was set at 25–75mv/s. As shown in Fig. 3B, the current peak of the redox reaction is positively linearly related to the scan rate range. The linear relationship between the oxidation peak (I_{pa}) and reduction peak (I_{pc}) currents and the square root of the scan rate ($v^{1/2}$) is shown in Fig. 3C. The linear equations were determined to be $I_{pa} = 5.16 v^{1/2} (mV s^{-1}) − 6.56 (R^2 = 0.9953)$ and $I_{pc} = −4.83 v^{1/2} (mV s^{-1}) + 4.56 (R^2 = 0.9965)$. These results showed that the reaction on the surface of immunosensor was a diffusion-controlled surface reaction.

3.2 The feasibility of the prepared sensor for detecting AFB$_1$

The feasibility of the prepared sensor for detecting AFB$_1$ was studied. After modification with COOH−GO−COOH−MWNT (curve b, Fig. 4A), the peak current is higher than that of the unmodified electrode (curve a). It has been reported that in the composite of GO−MWNT, MWNTs can avoid the aggregation of GO sheets, and GO nanosheets can help to disperse MWNTs to form a three-dimensional networks. Therefore, the combination of GO and MWNT can often lead to good synergy effect for electrochemical sensors. In addition, the carboxylation of these two carbon materials leads to a large number of carboxyl

functional groups on their surfaces, which leads to higher hydrophilicity and biocompatibility, thus further improving the performance of sensor. After pDA (curve c) and AuNPs (curve d) was electrodeposited and polymerized on the electrode, peak current was increased further. pDA has abundant functional groups and excellent biocompatibility. It also can effectively amplify charge transfer of mediators.[24,25] AuNPs have also been frequently studied for amplifying the electric signal due to their large specific surface area and good conductivity. Therefore, peak current was increased further after pDA (curve c) and AuNPs (curve d) were modified on the electrode surface. Then the aptamer (curve e, Fig. 4B) and MCH (curve f) was immobilized on the electrode, the peak current becomes smaller, because the aptamer and MCH was both insulated, thus hindering the transfer of signal molecules to the electrode surface. After AFB$_1$ was immobilized on the modified electrode, the peak current decreased again (curve g). It has been reported that after binding with AFB$_1$, the aptamer will undergoes a conformational change to form a hairpin structure, so the modified layer on the electrode surface becomes more compact.[37,38] In addition, the AFB$_1$ is also insulated. Therefore, after the binding of AFB$_1$, the peak current decreased again. This result suggests that AFB$_1$ can be detected by the prepared sensor.

A control sensor without the modification of COOH−GO−COOH−MWNT nanocomposite and pDA was also prepared. The AuNPs can't be omitted as they must be used to bind with the −SH contained aptamers. The prepared MCH/SH-Apt/Au/pDA/COOH−GO−COOH−MWNT/SPE and control sensor were both incubated with 100 fg mL^{-1} AFB$_1$. The change of peak current ΔI before and after incubation with AFB$_1$ was compared ($\Delta I = I_{MCH} − I_{AFB_1}$). As shown in Fig. 4C, ΔI of MCH/SH-Apt/Au/pDA/COOH−GO−COOH−MWNT/SPE was nearly 3 times as that of control sensor, which confirmed the application of COOH−GO−COOH−MWNT nanocomposite and pDA can effectively improve the sensing performance of the prepared AFB1 sensor.

3.3 Optimization for the AFB$_1$ sensor

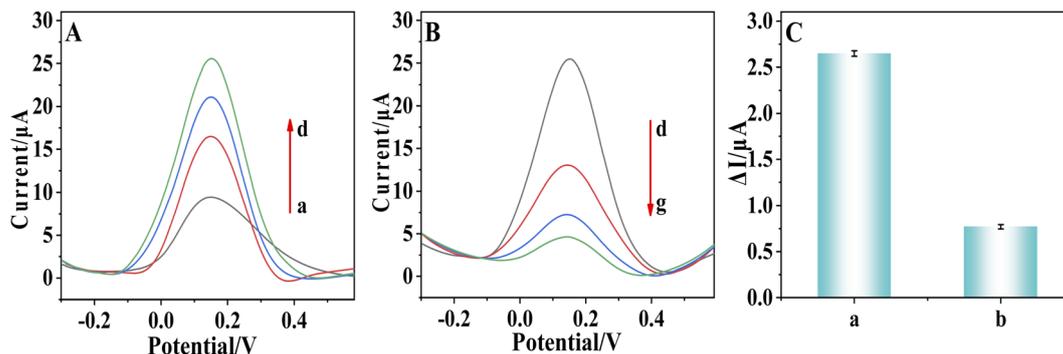The effect of the deposition time of AuNPs on the experiment was investigated. The amount of AuNPs on the surface of the

Fig. 4 (A) DPV curves of bare SPE (a), COOH–GO–COOH–MWNT/SPE (b), pDA/COOH–GO–COOH–MWNT/SPE (c) and Au/pDA/COOH–GO–COOH–MWNT/SPE (d) in the presence of 5 mM $[Fe(CN)_6]^{3-/4-}$ in 0.01 M PBS (pH 7.5, containing 0.1 M KCl). (B) DPV curves of Au/pDA/COOH–GO–COOH–MWNT/SPE (d), SH-Apt/Au/pDA/COOH–GO–COOH–MWNT/SPE (e), MCH/SH-Apt/Au/pDA/COOH–GO–COOH–MWNT/SPE (f) and AFB$_1$/MCH/SH-Apt/Au/pDA/COOH–GO–COOH–MWNT/SPE (g) in the presence of 5 mM $[Fe(CN)_6]^{3-/4-}$ in 0.01 M PBS (pH 7.5, containing 0.1 M KCl). (C) Comparison of ΔI of the MCH/SH-Apt/Au/pDA/COOH–GO–COOH–MWNT/SPE (a) and the control MCH/SH-Apt/Au/SPE (b) after binding with AFB$_1$.

SPE electrode can be controlled by controlling the electrodeposition time. As shown in Fig. S1A,† ΔI gradually increases from 800 to 1000 s, with the extension of time, ΔI decreases. Therefore, 1000 s was selected as the electrodeposition time.

The number of CV cycles affects the polymerization effect of DA. As can be seen from Fig. S1B,† ΔI gradually increases from 20 to 60 cycles, and begins to decline after 60 cycles. Therefore, the optimal CV cycles of dopamine polymerization is 60.

The effect of the concentration of aptamer on the sensor performance was investigated. When the aptamer concentration was increased from 0.25 μM to 1 μM, ΔI increased (Fig. S1C†). However, when the concentration of aptamers continued to increase, ΔI decreased, which may mean that the binding ability of the sensor for aptamer has reached saturation. Finally, it was concluded that the optimal concentration of aptamer was 1 μM.

The amount of COOH–GO–COOH–MWNT modification also affects the electrode performance. As shown in Fig. S1D,† ΔI increased as the droping volume increased from 3 μl to 4 μl. When the dropping volume increases further, ΔI showed an obvious downward trend, so the dropping volume of COOH–GO–COOH–MWNT was selected to be 4 μl.

The deposition potential also affects the deposition effect of gold nanoparticles. It can be seen from Fig. S1E† that the ΔI increases from −1.7 V to −1.3 V, and ΔI gradually decreases as the potential continues to increase. Therefore, we determined that −1.3 V is the best potential for gold deposition.

The ratio of COOH–GO to COOH–MWNT also has an important impact on the performance of the electrode, as shown in Fig. S1F,† When the ratio of COOH–GO to COOH–MWNT is 2 : 2, ΔI reaches the maximum value. Therefore, 2 : 2 was selected as the optimal ratio of COOH–GO to COOH–MWNT. Based on this ratio, the concentration of COOH–GO–COOH–MWNT nanocomposites was also optimized. As shown in Fig. S1G,† when the concentration of nanomaterials increases to 1 mg ml^{-1}, ΔI reaches a maximum value. When the concentration of nanomaterials continue to increase, ΔI begin to decrease. So that 1 mg ml^{-1} was the optimal concentration for COOH–GO–COOH–MWNT nanocomposites.

The pH value of the electrolyte directly affects the effect of the test. Electrolytes with different pH values were used for the test. The results are shown in Fig. S1H.† For the electrolyte with pH values from 6 to 7.5, ΔI gradually increases. When the pH value of electrolyte continue to rise, ΔI begin to decrease. So that pH 7.5 was used as the optimal pH for the electrolyte.

3.4 The performance of the AFB$_1$ sensor

The prepared sensors were incubated with different concentrations of AFB$_1$(0.1 fg ml^{-1}–100 pg ml^{-1}). The results for each AFB$_1$ concentration are shown in Fig. 5A. The oxidation peak current decreases with the increasing concentration of AFB$_1$ because the aptamer–toxin complex hindered the transfer of signal molecules to the electrode surface. The change of current response (ΔI) was positively correlated with the concentration of AFB$_1$ in the range of 0.1 fg ml^{-1} to 100 pg ml^{-1}, and the regression equation is $\Delta I (\mu A) = 0.5637...\log C_{AFB_1} (fg\ ml^{-1}) + 1.5073$ and the correlation coefficient (R^2) is 0.9880. The LOD reached 15.14 ag ml^{-1} (S/N = 3). The LOD and linear range of the prepared sensor is comparable to or better than some AFB$_1$ sensors previously reported[39–45] (Table S1†). The high performance of the prepared sensors is mainly due to that the application of COOH–GO–COOH–MWNT nanocomposite, pDA and AuNPs greatly increases the surface activity area, conductivity and biocompatibility of the sensor.

The prepared sensor is used to detect 100 fg ml^{-1} of AFB$_2$, OTB, FB$_1$, FB$_2$, ZON, and DON, respectively. The results are shown in Fig. 6. ΔI of the sensor for other interfering substances is significantly lower than that of AFB$_1$, and it can be concluded that the selectivity of the sensor is excellent. The prepared sensor detected the same AFB$_1$ solution for 6 times, the RSD was 6.62% (Fig. S2†). Six sensors were used to detect the same AFB$_1$ solution, and the RSD was 7.25% (Fig. S3†). In addition, the prepared sensors were stored in the refrigerator for two weeks, and the same concentration of AFB$_1$ were detected every two days. The RSD of the 14 days measurement results was 8.09% (Fig. S4†). The test results prove the high stability and reproducibility of the sensor.
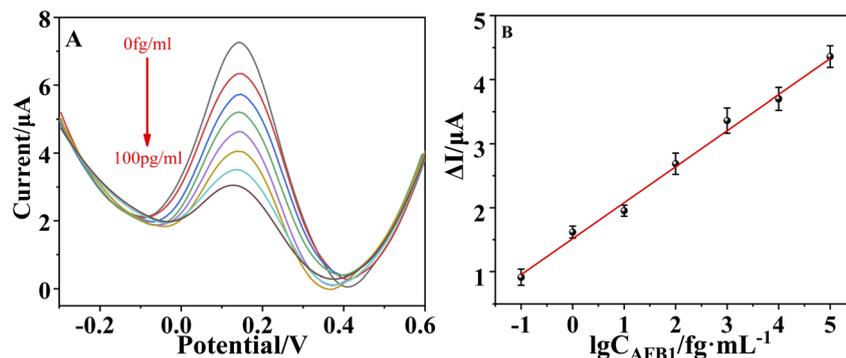
Fig. 5 (A) DPV responses of the aptasensor after 60 min incubation with 0, 0.0001, 0.001, 0.01, 0.1,1, 10 and 100 pg mL^{-1} AFB$_1$. (B) The calibration plot for ΔI and the logarithm of AFB$_1$ concentration.
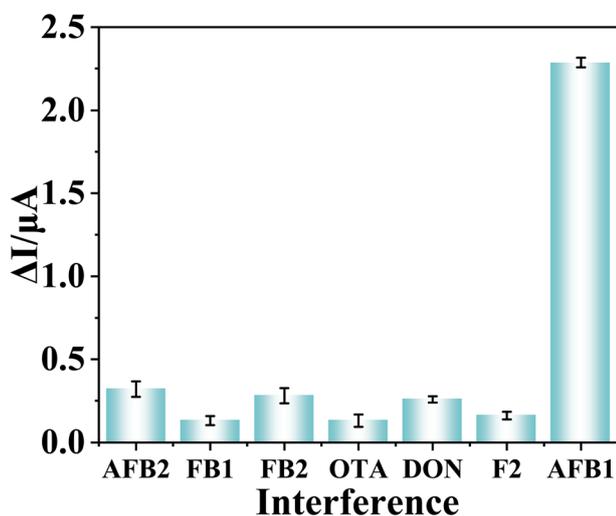

Fig. 6 Sensor responses to different interferences at 100 fg ml^{-1}.

Table 1 The recoveries of AFB1 in milk samples ($n = 3$).

Added AFB$_1$ (pg ml^{-1})	Found (pg ml^{-1})	Recovery (%)	RSD (%)
0.1	0.10	102.49%	6.90%
1	0.94	94.21%	7.53%
10	10.05	100.51%	12.51%

3.5 Real sample analysis

To verify the practicability of this sensor, it was applied to detect AFB$_1$ in milk, which was purchased from local supermarket. The milk was diluted and different concentration of AFB$_1$ was spiked.[46,47] As shown in Table 1, the recoveries are 102.49%, 94.21% and 100.51%, respectively. The results show that the sensor has great application potential for monitoring AFB$_1$ in real samples.

4 Conclusions

In summary, an aptamer electrochemical sensor for AFB$_1$ detection was developed based on COOH–GO–COOH–MWNT

nanocomposites, pDA and AuNPs fabricated SPE electrode. Due to the excellent catalytic activity, biocompatibility and electrochemical stability of the nanomaterials, and high affinity and specific recognition capabilities of the aptamers, the as-prepared electrochemical AFB$_1$ sensor not only has low LOD, wide linear range, excellent selectivity and stability, but also is simple and low cost, which could be considered as a promising tool towards AFB$_1$ detection in practical application.

Conflicts of interest

There are no conflicts to declare.

Acknowledgements

References

1 Y. Li, D. Liu, S. Meng, T. Chen, C. Liu and T. You, *Biosens. Bioelectron.*, 2022, **195**, 113634.
2 Y. Chen, F. Zhang, R. Liu, M. Liu, Y. Sang, S. Wang and X. Wang, *Foods*, 2021, **10**, 2568–2574.
3 W. Zheng, J. Teng, L. Cheng, Y. Ye, D. Pan, J. Wu, F. Xue, G. Liu and W. Chen, *Biosens. Bioelectron.*, 2016, **80**, 574–581.
4 F. S. Sabet, M. Hosseini, H. Khabbaz, M. Dadmehr and M. R. Ganjali, *Food Chemistry*, 2017, **220**, 527–532.
5 G. Castillo, K. Spinella, A. Poturnayová, M. Šnejdárková, L. Mosiello and T. Hianik, *Food Control*, 2015, **52**, 9–18.
6 J. Li, X. Fang, Y. Yang, X. Cheng and P. Tang, *Food Analytical Methods*, 2016, **9**, 3080–3086.
7 A. M. Beyene, X. Du, E. S. Dwayne, S. Ensley and W. K. Rumbeiha, *BMC Res. Notes*, 2019, **12**, 492.
8 J. Li, X. Xu, W. Guo, Y. Zhang, X. Feng and F. Zhang, *Food Chemistry*, 2022, **387**, 132821.
9 C. Wang, L. Zhang, J. Luo, J. Qin, J. Jiang, L. Qin, Z. Zhao, S. Yang and M. Yang, *Toxicon*, 2021, **197**, 99–105.

10 F. Jahangiri-Dehaghani, H. R. Zare, Z. Shekari and A. Benvidi, *Anal. Bioanal. Chem.*, 2022, **414**, 1973–1985.

11 L. Lan, Y. Yao, J. Ping and Y. Ying, *ACS Appl. Mater. Interfaces*, 2017, **9**, 23287–23301.

12 C. Wang, W. Zhang, J. Qian, L. Wang, Y. Ren, Y. Wang, M. Xu and X. Huang, *Anal. Methods*, 2021, **13**, 462–468.

13 C. Zhu, D. Liu, Y. Li, T. Chen and T. You, *Food Chemistry*, 2022, **373**, 131443.

14 C. Liu, T. Wu, W. Zeng, J. Liu, B. Hu and L. Wu, *Sens. Actuators, B*, 2022, **371**, 132494.

15 Q. Huang, X. Lin, D. Chen and Q. X. Tong, *Food Chemistry*, 2022, **373**, 131415.

16 L. Wu, F. Ding, W. Yin, J. Ma, B. Wang, A. Nie and H. Han, *Anal. Chem.*, 2017, 101399.

17 Z. Suo, X. Liang, H. Jin, B. He and M. Wei, *Anal. Bioanal. Chem.*, 2021, **413**, 7587–7595.

18 L. Wu, M. Zhou, Y. Wang and J. Liu, *J. Hazard. Mater.*, 2020, **399**, 123154.

19 A. Ravalli, D. Voccia, I. Palchetti and G. Marrazza, *Biosensors*, 2016, **6**, 39–44.

20 F. Hong, C. Huang, L. Wu, M. Wang, Y. Chen and Y. She, *Biosens. Bioelectron.*, 2021, **192**, 113489.

21 N. Razmi, B. Baradaran, M. Hejazi, M. Hasanzadeh, J. Mosafer, A. Mokhtarzadeh and M. de la Guardia, *Biosens. Bioelectron.*, 2018, **113**, 58–71.

22 A. Vasilescu and J.-L. Marty, *Trends Anal. Chem.*, 2016, **79**, 60–70.

23 M. Yousefi, S. Dehghani, R. Nosrati, H. Zare, M. Evazalipour, J. Mosafer, B. S. Tehrani, A. Pasdar, A. Mokhtarzadeh and M. Ramezani, *Biosens. Bioelectron.*, 2019, **130**, 1–19.

24 H. Shan, X. Li, L. Liu, D. Song and Z. Wang, *J. Mater. Chem. B*, 2020, **8**, 5808–5825.

25 K. Abnous, N. M. Danesh, M. Alibolandi, M. Ramezani, A. Sarreshtehdar Emrani, R. Zolfaghari and S. M. Taghdisi, *Biosens. Bioelectron.*, 2017, **94**, 374–379.

26 C. Wang, Y. Li and Q. Zhao, *Biosens. Bioelectron.*, 2019, **144**, 111641.

27 C. Wu, X. Huang, X. Wu, L. Xie, K. Yang and P. Jiang, *Nanoscale*, 2013, **5**, 3847–3855.

28 P. Chen, T. Y. Xiao, Y. H. Qian, S. S. Li and S. H. Yu, *Adv. Mater.*, 2013, **25**, 3192–3196.

29 B. You, L. Wang, L. Yao and J. Yang, *Chem. Commun.*, 2013, **49**, 5016–5018.

30 G. Xing, B. Luo, J. Qin, X. Wang, P. Hou, H. Zhang, C. Wang, J. Wang and A. Li, *Talanta*, 2021, **232**, 122477.

31 K. Liu, X. Wang, B. Luo, C. Wang, P. Hou, H. Dong, A. Li and C. Zhao, *Frontiers in Plant Science*, 2022, **13**, 872190.

32 E. Kim, Y. Xiong, Y. Cheng, H.-C. Wu, Y. Liu, B. Morrow, H. Ben-Yoav, R. Ghodssi, G. Rubloff, J. Shen, W. Bentley, X. Shi and G. Payne, *Polymers*, 2014, 7, 1–46.

33 E. Kim, T. E. Winkler, C. Kitchen, M. Kang, G. Banis, W. E. Bentley, D. L. Kelly, R. Ghodssi and G. F. Payne, *Anal. Chem.*, 2017, **89**, 1583–1592.

34 C. Wang, L. Liu and Q. Zhao, *ACS Sens.*, 2020, **5**, 3246–3253.

35 Y. Li, L. Sun and Q. Zhao, *Anal. Bioanal. Chem.*, 2018, **410**, 6269–6277.

36 Z. Lu, D. Hou, A. Hanif, W. Hao, Z. Li and G. Sun, *Cem. Concr. Compos.*, 2018, **94**, 33–42.

37 D. Wu, *Int. J. Electrochem. Sci.*, 2022, 220948, DOI: **10.20964/2022.09.33**.

38 G. S. Geleta, Z. Zhao and Z. Wang, *Analyst*, 2018, **143**, 1644–1649.

39 C. Zhu, D. Liu, Y. Li, S. Ma, M. Wang and T. You, *Biosens. Bioelectron.*, 2021, **174**, 112654.

40 T. Chen, Y. Li, S. Meng, C. Liu, D. Liu, D. Dong and T. You, *Talanta*, 2022, **242**, 123280.

41 G. S. Geleta, Z. Zhao and Z. Wang, *Analyst*, 2018, **143**, 1644–1649.

42 T. Zhong, S. Li, X. Li, Y. JiYe, Y. Mo, L. Chen, Z. Zhang, H. Wu, M. Li and Q. Luo, *Food Chemistry*, 2022, **384**, 132495.

43 Y. Li, D. Liu, C. Zhu, X. Shen, Y. Liu and T. You, *J. Hazard. Mater.*, 2020, **387**, 122001.

44 H. Cui, K. An, C. Wang, Y. Chen, S. Jia, J. Qian, N. Hao, J. Wei and K. Wang, *Sens. Actuators, B*, 2022, **355**, 131238.

45 G. Selvolini, M. Lettieri, L. Tassoni, S. Gastaldello, M. Grillo, C. Maran and G. Marrazza, *Talanta*, 2019, **203**, 49–57.

46 K. Yang, Z. Yan, L. Ma, Y. Du, B. Peng and J. Feng, *Nanomaterials*, 2019, **9**, 523–531.

47 C. Wang and Q. Zhao, *Biosens. Bioelectron.*, 2020, **167**, 112478.